Wave Motion 93 (2020) 102446

Contents lists available at ScienceDirect

Wave Motion

journal homepage: www.elsevier.com/locate/wamot

Wave propagation in double helical rods

Jamil Renno *, Sadok Sassi, Samer Gowid

Department of Mechanical & Industrial Engineering, College of Engineering, Qatar University, Doha, Qatar

ARTICLE INFO

Article history:
Received 21 May 2019
Received in revised form 6 October 2019
Accepted 14 October 2019
Available online 25 October 2019

Keywords:
Double helix
Wave propagation
Wave and finite element method
Fractal behaviour

ABSTRACT

The propagation of waves in helical rods has been studied extensively. However, studying the wave propagation in double helical rods have received less attention although this can be useful in multiple fields of science and engineering. Obtaining an analytical model for a double helical rod is challenging since the curvature and tortuosity are not constant. Thus, resolving the wave behaviour analytically is nearly impossible. In this paper, wave propagation in a double helical rod will be studied using the wave and finite element method which is a technique that can be used to model homogeneous and periodic one and two dimensional structures based on the periodic structure theory. For modelling a double helical rod, the finite element model of a single turn is processed using Bloch waves. The dispersion curves and wavemodes are obtained and the similarities and differences of waves in helical and double helical rods are highlighted.

1. Introduction

The propagation of elastic waves in helical rods with canonical (i.e., square or circular) cross-sections have been studied extensively in the literature starting with the classical work of Love [1]. The effect of shear deformation and rotary inertia in a helical rod were added in [2] and formed the basis of the finite element model that was presented in [3] and the pseudospectral model that was developed in [4,5]. Treyssède used a semi-analytical finite element method to study wave propagation in helical waveguides [6] and to examine the energy flux in these structures in the context of non-destructive testing [7]. Sorokin used the model in [2] to investigate the wave propagation in helical rods using asymptotic analyses [8] and then used the Green's matrix and boundary integral equations to study the time-harmonic dynamics of helical rods [9]. Liu et al. [10] used the scaled boundary finite element method to investigate the dispersion properties of helical waveguides. Recently, Maurin et al. used Bloch's theorem to study wave propagation in waveguides with screw and glide periodicities [11].

The modelling of double helical rods has received less attention in the literature. A double helical rod is a rod whose central axis is a secondary helix that is coiled around a primary helix. In other words, the aforementioned central axis of the double helical rod is a fractal structure of the second order [12]. The vibration of a double helical rod is relevant at the molecular level in biological structures [13,14]. The wave propagation in helices and hyperhelices was studied by [12] who used a fractal regression approach to analyse wave propagation and show that they also have fractal attributes. One of the motivations to study wave propagation of super and hyperhelices is that the study of the dynamics of such rods might provide a useful analogy for advancing the understanding of string theory [15].

As for the governing equations of a helical rod, these can be obtained with varying degrees of complexity. A thorough discussion of the suitability and frequency-range of applicability of the various modelling approaches is presented in [8].

* Corresponding author.
E-mail addresses: jamil.renno@qu.edu.qa (J. Renno), sadok.sassi@qu.edu.qa (S. Sassi), samer@qu.edu.qa (S. Gowid).

https://doi.org/10.1016/j.wavemoti.2019.102446
0165-2125/

Nomenclature

E	Young's modulus, N/m^2
N	Number of turns of the primary helix, dimensionless
R_1	Radius of the primary helix, m
R_2	Radius of the double helix, m
$\imath$	Unit imaginary number, $\sqrt{-1}$
κ_1	Curvature of the primary helix, 1/m
κ_2	Curvature of the double helix, 1/m
ψ	Pitch angle of the primary helix, rad
ρ	Density, kg/m^3
τ_1	Tortuosity of the primary helix, 1/m
τ_2	Tortuosity of the double helix, 1/m
θ	Phase angle of the double helix, rad
c	Speed of plane dilation wave in the rod's material, m/s
d	Diameter of circular rod, m
h	Pitch of the primary helix, m
l_1	Length of one turn of the primary helix, m
l_2	Length of one turn of the double helix, m
p	Number of turns of the double helix around one turn of the primary helix, dimensionless
s	Curvilinear abscissa, m

Superscripts

$\pm$	Positive/negative going wave

Subscripts

g	Quantity expressed in the global coordinate system
I	Quantity pertaining to internal nodes
L	Quantity pertaining to left nodes (or boundary)
R	Quantity pertaining to right nodes (or boundary)

However, the governing equations of a double helical rod are too cumbersome to develop (especially as shown later since many of the geometric properties do not posses translational invariance). Even calculating the length of a double helical path, which has applications in shape sensing of deformable cylinders [16], endoscopes [17] and multicore optical fibres [18], cannot be performed analytically owing to its complexity [19].

In this paper, the wave propagation in a double helical rod is considered using the wave and finite element (WFE) method. The WFE method applies the periodicity theory to the finite element (FE) model of a small segment of a waveguide to formulate an eigenvalue problem whose solution provides the wavenumbers and wavemodes of the waveguide [20–23]. The WFE method have also been used to investigate the scattering of waves in two-dimensional structures [24] and to study the wave behaviour of pipes with helical characteristics [25] and helically orthotropic cylindrical shells and lattices [26].

The remainder of this paper is organized as follows. The geometric characteristics of a double helix are discussed in Section 2. This forms the basis for obtaining the finite element model of a single turn of the double helical rod and the WFE model. To this end, Section 3 presents free and forced wave propagation. Numerical examples are presented in Section 4. Conclusions for this work are drawn in Section 5.

2. Geometry of a double helix

The formulation starts with a discussion of the geometry of a double helix. The primary helix can be parametrized by the following position vector

$$\vec{r}_1(s) = R_1 \cos(\epsilon_1 s)\,\hat{i} + R_1 \sin(\epsilon_1 s)\,\hat{j} + \frac{h}{l_1} s\hat{k}\,, \tag{1}$$

where $\hat{i}, \hat{j}$ and $\hat{k}$ are the unit vectors of the global coordinate system (x, y, z) and

$$\epsilon_1 = \frac{2\pi}{l_1} \quad , \quad l_1 = \sqrt{h^2 + 4\pi^2 R_1^2}.$$

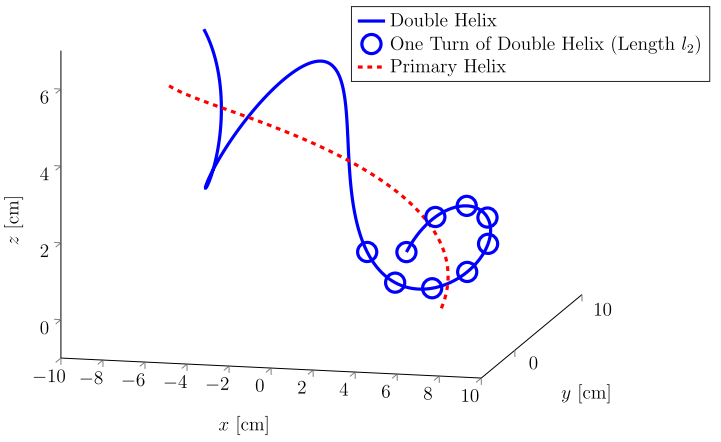

Fig. 1. A double helix with $R_1 = 6.5$ cm, $R_2 = R_1/3$, $\psi = 0.13$ rad, $\theta = \pi/4$ rad; only half a turn of the primary helix is shown.

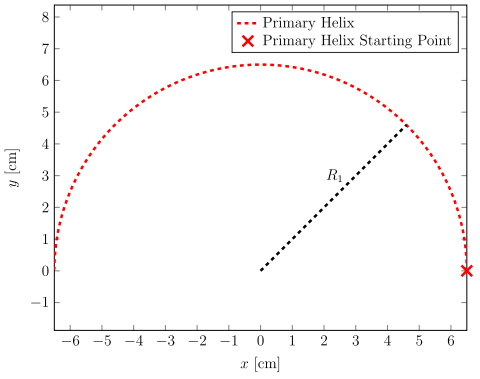

(a) x-y view of the primary helix showing its radius R_1.

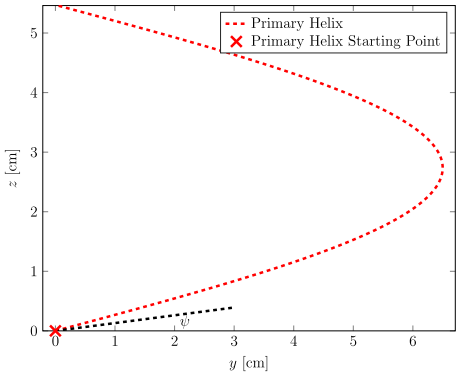

(b) x-z view of the primary helix which shows the helix angle ψ; the height of the helix in this case is $h/2$.

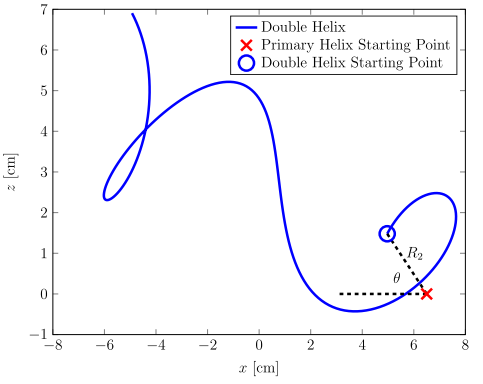

(c) x-z view of the double helix showing its radius R_2 and the phase angle of the double helix θ.

Fig. 2. Different views of the double helix shown in Fig. 1.

The pitch of the primary helix h is related to the helix angle ψ by

$$h = 2\pi R_1 \tan(\psi)\ . \tag{2}$$

A complete turn of the primary helix is described by the curvilinear abscissa s varying from 0 to l_1.

The double helix is parametrized by

$$\vec{r}_2(s) = \vec{r}_1(s) + R_2 \cos(\epsilon_2 s + \theta)\, \hat{n}_1(s) + R_2 \sin(\epsilon_2 s + \theta)\, \hat{b}_1(s)\ , \tag{3}$$

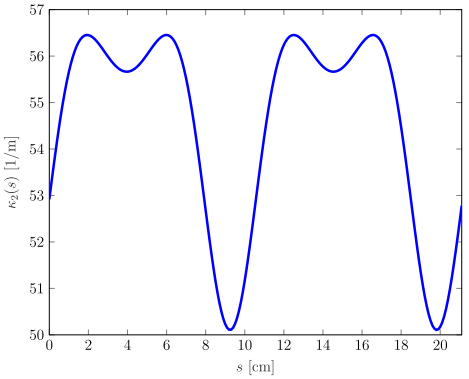

(a) Curvature of the double helix over two turns (of the double helix).

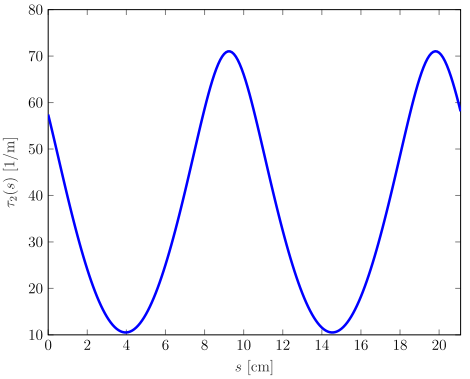

(b) Tortuosity of the double helix over two turns (of the double helix).

Fig. 3. Geometric properties of the double helix shown in Fig. 1.

where

$$\epsilon_2 = p\,\epsilon_1 \quad , \quad p \in \mathbb{R}_{>0}\ .$$

Fig. 1 shows a plot of a double helix along with the primary helix. Fig. 2 shows different views of the double and primary helices with annotations showing the radius of the primary helix, R_1, the radius of the double helix, R_2, the phase angle of the double helix, θ, and the helix angle, ψ, which is related to the pitch of the helix h defined in Eq. (2). Vectors $\hat{n}_1$ and $\hat{b}_1$ in Eq. (3) are the normal and binormal unit vectors of the primary helix. For both the primary and double helices, the tangential, normal and binormal unit vectors are defined as

$$\hat{t}_i(s) = \frac{1}{\left\| \frac{\mathrm{d}\vec{r}_i}{\mathrm{d}s} \right\|} \frac{\mathrm{d}\vec{r}_i}{\mathrm{d}s} \quad , \quad \hat{n}_i(s) = \frac{1}{\left\| \frac{\mathrm{d}\hat{t}_i}{\mathrm{d}s} \right\|} \frac{\mathrm{d}\hat{t}_i}{\mathrm{d}s} = \frac{1}{\kappa_i(s)} \frac{\mathrm{d}\hat{t}_i}{\mathrm{d}s} \quad \text{and} \quad \hat{b}_i(s) = \hat{t}_i(s) \times \hat{n}_i(s)\ , \tag{4}$$

with $i = 1, 2$ corresponding to the primary and secondary helix, respectively. The normal vector, $\hat{n}_i(s)$, (in Eq. (4)) is defined by one of the three Frenet–Serret formulae; the other two formulae are

$$\frac{\mathrm{d}\hat{n}_i}{\mathrm{d}s} = \tau_i(s)\hat{b}_i(s) - \kappa_i(s)\hat{t}_i(s) \quad \text{and} \quad \frac{\mathrm{d}\hat{b}_i}{\mathrm{d}s} = -\tau_i(s)\hat{n}_i(s)\ . \tag{5}$$

The curvature and tortuosity of the primary helix are constants

$$\kappa_1 = \frac{4\pi^2 R_1}{l_1^2}\ ,\ \tau_1 = \frac{2\pi h}{l_1^2}\ .$$

However, for the double helix, the curvature and tortuosity (κ_2 and τ_2, respectively) are functions of the curvilinear coordinate s. The expression of κ_2 and τ_2 can be obtained using symbolic manipulation software packages, e.g. MATHEMATICA [27]. The expression of $\kappa_2(s)$ is presented in Appendix; the expression of $\tau_2(s)$ is too cumbersome to be included herein. Both the curvature and tortuosity of the double helix, however, are periodic with respect to the curvilinear coordinate s. Figs. 3a and 3b show the curvature and tortuosity of a double helix with $R_1 = 3R_2$, $\theta = \pi/4$, $p = 4$ and $\psi = 0.13$ over two turns of the double helix.

Due to the variation in the curvature and tortuosity, a double helical rod cannot be considered as a homogeneous waveguide. It is rather a periodic waveguide where the period is a single turn of the double helix whose length is

$$l_2 = \int_0^{s_2} \sqrt{\frac{\mathrm{d}\vec{r}_2}{\mathrm{d}s} \cdot \frac{\mathrm{d}\vec{r}_2}{\mathrm{d}s}}\mathrm{d}s \quad \text{where} \quad s_2 = \frac{2\pi - \theta}{\epsilon_2}\ . \tag{6}$$

Using Eqs. (4) and (5), Eq. (6) can be simplified to

$$l_2 = \int_0^{s_2} \sqrt{[1 - R_2\kappa_1 \cos(\epsilon_2 s + \theta)]^2 + [R_2(\epsilon_2 + \tau_1)]^2}\mathrm{d}s\ . \tag{7}$$

The integral in Eq. (7) cannot be solved in closed-form although this can have many useful applications. Recently, a numerical approach that uses a Maclaurin-type series expansion was proposed to calculate the length of a double helix [19]; however, the convergence speed could be further improved.

Eq. (1) can be parametrized in terms of the curvature and tortuosity of the primary helix since the following holds

$$R_1 = \frac{\kappa_1}{\kappa_1^2 + \tau_1^2}\ ,\ \epsilon_1 = \sqrt{\kappa_1^2 + \tau_1^2}\ ,\ h = \frac{\tau_1}{\epsilon_1}\ . \tag{8}$$

Using Eq. (1) through Eq. (4) along with Eq. (8), transformation matrices can be obtained between the local coordinate systems and the global coordinate system

$$\begin{Bmatrix} \hat{t}_i \\ \hat{n}_i \\ \hat{b}_i \end{Bmatrix} = \mathbf{R}_i \begin{Bmatrix} \hat{i} \\ \hat{j} \\ \hat{k} \end{Bmatrix}\ . \tag{9}$$

The transformation matrix between the $(\hat{t}_1, \hat{n}_1, \hat{b}_1)$ coordinate system and the global coordinate system is

$$\mathbf{R}_1(s) = \frac{1}{\epsilon_1}\begin{bmatrix} -\kappa_1 \sin(\epsilon_1 s) & \kappa \cos(\epsilon_1 s) & \tau_1 \\ -\epsilon_1 \cos(\epsilon_1 s) & -\epsilon_1 \sin(\epsilon_1 s) & 0 \\ \tau_1 \sin(\epsilon_1 s) & -\tau_1 \cos(\epsilon_1 s) & \kappa_1 \end{bmatrix}\ .$$

Symbolic manipulation software packages, e.g. MATHEMATICA [27], can be used to obtain $\mathbf{R}_2(s)$; however, similar to $\tau_2(s)$, the expressions of the elements of $\mathbf{R}_2(s)$ are too cumbersome to present herein.

3. Wave propagation

Given the complexity of the geometry of the double helical rod, it is a formidable task to develop the governing equations and hence resolve the wave behaviour analytically. Thus, the wave and finite element (WFE) will be used to analyse the wave behaviour of a double helical rod. The WFE method has been used to model the free [22] and forced vibration [23,28] of straight and curved [29] waveguides. The WFE have also been used to model wave propagation in helical rods [30] and to model the power flow and scattering in helical waveguides [31].

The location of any point on the centreline of the double helical rod is described by Eq. (3) and the local displacements (u, v, w) and rotations (α, β, γ) are defined along and about the $(\hat{t}_2, \hat{n}_2, \hat{b}_2)$ coordinate system, respectively.

3.1. Review of the wave and finite element method

In this section, the WFE method for waveguides will be briefly reviewed based on the developments of [22,23] and adapted to the current treatment. First, free and then forced wave propagation will be reviewed followed by forced vibration.

3.1.1. Free wave propagation

Since the double helical rod is a periodic waveguide, the WFE model starts with obtaining the FE model of a single turn of the double helical rod (whose length is given in Eq. (7)). Straight beam elements are used to obtain the FE model of this periodic substructure. If n_s elements are used with increment Δs in the curvilinear coordinate, then the position vector of a point on the substructure is given as

$$\begin{aligned} \vec{r}_2\left((i-1)\Delta s\right) &= \vec{r}_1\left[(i-1)\Delta s\right] + R_2 \cos\left[(i-1)\epsilon_2 \Delta s + \theta\right] \hat{n}_1\left[(i-1)\Delta s\right] \\ &\quad + R_2 \sin\left[(i-1)\epsilon_2 \Delta s + \theta\right] \hat{b}_1\left[(i-1)\Delta s\right]\ , \end{aligned} \tag{10}$$

where $i = 1, \ldots, n_s + 1$. Note that the length of the ith element will be given as

$$\Delta e_i = \| \vec{r}_2(i\Delta s) - \vec{r}_2\left((i-1)\Delta s\right) \|\ . \tag{11}$$

The number of segments n_s used to discretize one turn of the double helical rod must be chosen such that

$$\sum_{i=1}^{n_s+1} \Delta e_i \approx l_2$$

where l_2 is given in Eq. (6). These elements are not of equal length (due to the dependence of the curvature and tortuosity of the double helix on the curvilinear coordinate s). Indeed, if $R_2 = 0$ (i.e., the centreline of the rod follows that of a standard helix), Δe_i simplifies to Δs (after using Eq. (3) and applying small angle approximation). The mass and stiffness matrices of these individual elements can be used to assemble the global mass and stiffness matrices of the single turn of the double helical rod in the global coordinate system. Each node in the beam element has 6 degrees of freedom (DOFs); thus, the model of the single turn will have $6 \times (n_s + 1)$ DOFs.

The resulting FE model (in the global coordinate system) under time harmonic motion of the form $\exp(-\imath\omega t)$ can be expressed in terms of the global dynamic stiffness matrix $\mathbf{D}_g = \left[\mathbf{K} - \omega^2\mathbf{M}\right]_g$ as

$$\begin{bmatrix} \tilde{\mathbf{D}}_{LL} & \tilde{\mathbf{D}}_{LI} & \tilde{\mathbf{D}}_{LR} \\ \tilde{\mathbf{D}}_{IL} & \tilde{\mathbf{D}}_{II} & \tilde{\mathbf{D}}_{IR} \\ \tilde{\mathbf{D}}_{RL} & \tilde{\mathbf{D}}_{RI} & \tilde{\mathbf{D}}_{RR} \end{bmatrix}_g \begin{Bmatrix} \mathbf{q}_L \\ \mathbf{q}_I \\ \mathbf{q}_R \end{Bmatrix}_g = \begin{Bmatrix} \mathbf{f}_L \\ \mathbf{f}_I \\ \mathbf{f}_R \end{Bmatrix}_g , \tag{12}$$

where, the dynamic stiffness matrix has been partitioned to reflect the contribution of the left, right and internal DOFs. If no external forces are applied to the internal nodes ($\mathbf{f}_I = \mathbf{0}$), the dynamic stiffness matrix can be condensed (dynamically) as

$$\begin{bmatrix} \mathbf{D}_{LL} & \mathbf{D}_{LR} \\ \mathbf{D}_{RL} & \mathbf{D}_{RR} \end{bmatrix}_g \begin{Bmatrix} \mathbf{q}_L \\ \mathbf{q}_R \end{Bmatrix}_g = \begin{Bmatrix} \mathbf{f}_L \\ \mathbf{f}_R \end{Bmatrix}_g , \tag{13}$$

where

$$\begin{bmatrix} \mathbf{D}_{LL} & \mathbf{D}_{LR} \\ \mathbf{D}_{RL} & \mathbf{D}_{RR} \end{bmatrix}_g = \begin{bmatrix} \tilde{\mathbf{D}}_{LL} & \tilde{\mathbf{D}}_{LR} \\ \tilde{\mathbf{D}}_{RL} & \tilde{\mathbf{D}}_{RR} \end{bmatrix}_g - \begin{bmatrix} \tilde{\mathbf{D}}_{LI} \\ \tilde{\mathbf{D}}_{RI} \end{bmatrix}_g \left[\tilde{\mathbf{D}}_{II}\right]_g^{-1} \begin{bmatrix} \tilde{\mathbf{D}}_{IL} & \tilde{\mathbf{D}}_{IR} \end{bmatrix}_g . \tag{14}$$

The dynamic stiffness matrix of Eq. (13) is of the size 12×12. Static condensation can also be used as discussed in [22]; however, static condensation is accurate only at low frequencies since the inertia associated with $\tilde{\mathbf{D}}_{II}$ is excluded. To transform the condensed model of the segment of Eq. (13), the rotation matrix $\mathbf{R}_2$ presented in Eq. (9) is used as

$$\begin{Bmatrix} \mathbf{q}_L \\ \mathbf{q}_R \end{Bmatrix}_g = \begin{bmatrix} \Theta_2^T(0) & \mathbf{0}_{6\times6} \\ \mathbf{0}_{6\times6} & \Theta_2^T(s_2) \end{bmatrix} \begin{Bmatrix} \mathbf{q}_L \\ \mathbf{q}_R \end{Bmatrix}_2 \text{ and } \begin{Bmatrix} \mathbf{f}_L \\ \mathbf{f}_R \end{Bmatrix}_g = \begin{bmatrix} \Theta_2^T(0) & \mathbf{0}_{6\times6} \\ \mathbf{0}_{6\times6} & \Theta_2^T(s_2) \end{bmatrix} \begin{Bmatrix} \mathbf{f}_L \\ \mathbf{f}_R \end{Bmatrix}_2 , \tag{15}$$

where

$$\Theta_2(s) = \begin{bmatrix} \mathbf{R}_2(s) & \mathbf{0}_{3\times3} \\ \mathbf{0}_{3\times3} & \mathbf{R}_2(s) \end{bmatrix} ,$$

and s_2 is given in Eq. (6). Note that only $\mathbf{R}_1$ is presented in Section 2; $\mathbf{R}_2(s)$ can be obtained using mathematical manipulation software [27] and its elements are too cumbersome to present in this paper. Using the transformation of Eq. (15) in Eq. (13) results into

$$\begin{bmatrix} \mathbf{D}_{LL} & \mathbf{D}_{LR} \\ \mathbf{D}_{RL} & \mathbf{D}_{RR} \end{bmatrix}_2 \begin{Bmatrix} \mathbf{q}_L \\ \mathbf{q}_R \end{Bmatrix}_2 = \begin{Bmatrix} \mathbf{f}_L \\ \mathbf{f}_R \end{Bmatrix}_2 , \tag{16}$$

where

$$\begin{bmatrix} \mathbf{D}_{LL} & \mathbf{D}_{LR} \\ \mathbf{D}_{RL} & \mathbf{D}_{RR} \end{bmatrix}_2 = \begin{bmatrix} \Theta_2(0) & \mathbf{0}_{6\times6} \\ \mathbf{0}_{6\times6} & \Theta_2(s_2) \end{bmatrix} \begin{bmatrix} \mathbf{D}_{LL} & \mathbf{D}_{LR} \\ \mathbf{D}_{RL} & \mathbf{D}_{RR} \end{bmatrix}_g \begin{bmatrix} \Theta_2^T(0) & \mathbf{0}_{6\times6} \\ \mathbf{0}_{6\times6} & \Theta_2^T(s_2) \end{bmatrix} .$$

In the sequel, the subscript "2" will be dropped for brevity. If a wave is propagating freely along the double helical rod, the propagation constant $\lambda = e^{-\imath k l_2}$ governs the relationship between the right and left nodal DOFs and forces as follows:

$$\mathbf{q}_R = \lambda\mathbf{q}_L \quad , \quad \mathbf{f}_R = -\lambda\mathbf{f}_L . \tag{17}$$

Substituting Eq. (17) into Eq. (16) yields an eigenvalue problem in λ. The eigenvalue problem can be cast in several forms, e.g.,

$$\lambda \begin{Bmatrix} \mathbf{q}_L \\ \mathbf{f}_L \end{Bmatrix} = \mathbf{T} \begin{Bmatrix} \mathbf{q}_L \\ \mathbf{f}_L \end{Bmatrix} \quad \text{where} \quad \mathbf{T} = \begin{bmatrix} -\mathbf{D}_{LR}^{-1}\mathbf{D}_{LL} & \mathbf{D}_{LR}^{-1} \\ -\mathbf{D}_{RL} + \mathbf{D}_{RR}\mathbf{D}_{LR}^{-1}\mathbf{D}_{LL} & -\mathbf{D}_{RR}\mathbf{D}_{LR}^{-1} \end{bmatrix} , \tag{18}$$

where $\mathbf{T}$ is referred to as the transfer matrix. Numerical problems might be encountered when solving this eigenvalue problem [22] and in that case, better-conditioned forms can be used [32].

The eigenvalues can be found in reciprocal pairs (i.e., λ_i^+ and $\lambda_i^- = 1/\lambda_i^+$), which have wavenumbers k_i^+ and $k_i^- = -k_i^+$ corresponding to the positive and negative going waves, respectively. The positive and negative going eigenvectors $\boldsymbol{\phi}_i^+$ and $\boldsymbol{\phi}_i^-$ (also called the wavemodes) are associated with the aforementioned eigenvalues. Each of the wavemodes can be partitioned as

$$\boldsymbol{\phi}_i = \begin{Bmatrix} \boldsymbol{\phi}_q \\ \boldsymbol{\phi}_f \end{Bmatrix}_i \quad \text{where} \quad i = 1, \ldots, 6 . \tag{19}$$

Positive going waves are characterized by

$$\begin{aligned} &\left|\lambda_i^+\right| \leq 1 , \\ &\Re\left(\mathbf{f}_L^T\dot{\mathbf{q}}_L\right) = \Re\left(\imath\omega\mathbf{f}_L^T\mathbf{q}_L\right) < 0 \quad \text{if} \quad \left|\lambda_i^+\right| = 1 , \end{aligned} \tag{20}$$

where the diacritic point is used to indicate a derivative with respect to time. Eq. (20) states that if the wave is travelling in the positive direction, then its amplitude should decrease or if the amplitude remains constant, then there must be

time-averaged power transmission in the positive direction. Eq. (20) includes evanescent waves that decay with increasing distance. Although these waves do not transfer energy, they contribute to the input response and they could give rise to propagating and evanescent waves when impinging on a discontinuity [33].

The following matrices can be used to group the wavemodes:

$$\mathbf{\Phi}^{\pm} = \begin{bmatrix} \boldsymbol{\phi}_1^{\pm} & \cdots & \boldsymbol{\phi}_6^{\pm} \end{bmatrix} \quad , \quad \mathbf{\Phi} = \begin{bmatrix} \mathbf{\Phi}^{+} & \mathbf{\Phi}^{-} \end{bmatrix} \ .$$

The left wavemodes, which are (1×12) vectors can also be partitioned as

$$\boldsymbol{\psi}_i = \begin{bmatrix} \boldsymbol{\psi}_f & \boldsymbol{\psi}_q \end{bmatrix}_i \quad \text{where} \quad i = 1, \ \ldots, 6 \ .$$

They can be grouped further as:

$$\mathbf{\Psi} = \begin{bmatrix} \mathbf{\Psi}^{+} \\ \mathbf{\Psi}^{-} \end{bmatrix} \quad \text{where} \quad \mathbf{\Psi}^{\pm} = \begin{bmatrix} \boldsymbol{\psi}_1^{\pm} \\ \vdots \\ \boldsymbol{\psi}_6^{\pm} \end{bmatrix} \ .$$

The left and right wavemodes can be normalized such that $\mathbf{\Psi}^{\pm}\mathbf{\Phi}^{\pm} = \mathbf{I}$. Further matrices can be formed from the partitions of the left and right wavemodes:

$$\mathbf{\Phi}_q^{\pm} = \begin{bmatrix} \boldsymbol{\phi}_{q,1}^{\pm} & \cdots & \boldsymbol{\phi}_{q,6}^{\pm} \end{bmatrix} \quad , \quad \mathbf{\Psi}_q^{\pm} = \begin{bmatrix} \boldsymbol{\psi}_{q,1}^{\pm} \\ \vdots \\ \boldsymbol{\psi}_{q,6}^{\pm} \end{bmatrix} \ .$$

Similar expressions exist for $\mathbf{\Phi}_f^{\pm}$ and $\mathbf{\Psi}_f^{\pm}$. These matrices, alongside the orthogonality relations, define the transformations between the physical domain and the wave domain as:

$$\begin{Bmatrix} \mathbf{q}_L \\ \mathbf{f}_L \end{Bmatrix} = \mathbf{\Phi}\mathbf{a} \quad \text{with} \quad \mathbf{a} = \begin{Bmatrix} \mathbf{a}^{+} \\ \mathbf{a}^{-} \end{Bmatrix} \ . \tag{21}$$

3.2. Forced wave propagation

A point load $\mathbf{f}_e$ that acts on the double helical rod generates positive- and negative-going waves of amplitudes ($\mathbf{e}^{+}$ and $\mathbf{e}^{-}$) that propagate away from the point load to the right and left, respectively. The amplitude of the excited waves can be calculated as

$$\mathbf{e}^{+} = \mathbf{\Psi}_q^{+}\mathbf{f}_e \quad \text{and} \quad \mathbf{e}^{-} = -\mathbf{\Psi}_q^{-}\mathbf{f}_e \ . \tag{22}$$

For spatially distributed loads, the amplitudes of the excited waves can be obtained analytically via the WFE model along with contour integration [23]. The knowledge of the excited waves can be further used to find the forced response of a finite double helical rod as laid out in the next subsection.

3.3. Forced response of finite double helical rod

The approach presented in [22] can be used to relate the travelling, incident and reflected waves to the excited waves of Eq. (22). Fig. 4 shows a schematic of a finite waveguide (e.g. the double helical rod considered herein) where $\mathbf{e}^{+}$ and $\mathbf{e}^{-}$ are the amplitudes of the excited waves that were computed in Eq. (22). The length of the double helical rod is Npl_2 where N is the number of turns of the primary helical path around which the centreline of the double helical rod is coiled and p and l_2 where introduced in Section 2. The double helical rod is excited at location s_e and the response is observed at s_r.

In general, the boundary conditions at the right and left boundaries can be expressed in terms of the DOFs and internal forces as

$$\mathbf{A}_{L,R}\mathbf{f} + \mathbf{B}_{L,R}\mathbf{q} = \mathbf{0}_{6\times 6} \ , \tag{23}$$

where matrices are $\mathbf{A}$ and $\mathbf{B}$ are matrices that may include stiffness, damping, etc. and may be complex and frequency dependent. For example, if the double helical rod is fixed at the left end, then $\mathbf{A}_L = \mathbf{0}_{6\times 6}$ and $\mathbf{B}_L = \mathbf{I}_{6\times 6}$. Using the form of Eq. (23) and writing the internal forces and DOFs in the wave basis of Eq. (21), the incident and reflected waves at the boundaries can be related as

$$\mathbf{d}^{+} = \mathbf{r}_L\mathbf{d}^{-} \quad \text{and} \quad \mathbf{c}^{-} = \mathbf{r}_R\mathbf{c}^{+} \ ,$$

where

$$\mathbf{r}_L = -\left(\mathbf{A}_L\mathbf{\Phi}_f^{+} + \mathbf{B}_L\mathbf{\Phi}_q^{+}\right)^{-1}\left(\mathbf{A}_L\mathbf{\Phi}_f^{-} + \mathbf{B}_L\mathbf{\Phi}_q^{-}\right) \ ,$$
$$\mathbf{r}_R = -\left(\mathbf{A}_R\mathbf{\Phi}_f^{-} + \mathbf{B}_R\mathbf{\Phi}_q^{-}\right)^{-1}\left(\mathbf{A}_R\mathbf{\Phi}_f^{+} + \mathbf{B}_R\mathbf{\Phi}_q^{+}\right) \ .$$

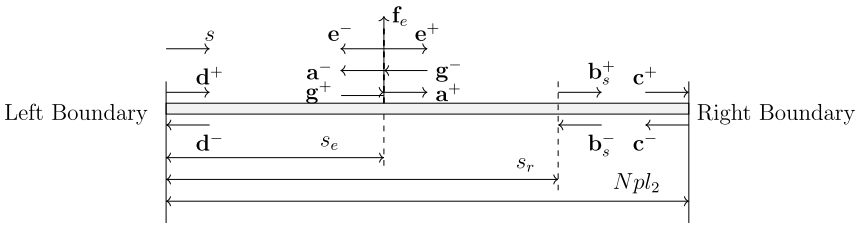

Fig. 4. Schematic of a waveguide excited by a point load showing the wave amplitudes at the excitation location s_e, the response location s_r and along with the incident and reflected waves at the boundaries.

The overall wave amplitude in the waveguide, $\mathbf{a}^{\pm}$, is the sum of the travelling waves $\mathbf{g}^{\pm}$ and the excited waves $\mathbf{e}^{\pm}$ as

$$\mathbf{a}^+ = \mathbf{e}^+ + \mathbf{g}^+ \quad \text{and} \quad \mathbf{g}^- = \mathbf{e}^- + \mathbf{a}^+ \ . \tag{24}$$

However, the amplitude of waves $\mathbf{g}^+$ contains the contribution of the left boundary as

$$\mathbf{g}^+ = \mathbf{F}(s_e)\mathbf{r}_L\mathbf{F}(s_e)\mathbf{g}^- \ ,$$

where $\mathbf{F}$ is the wave flight matrix given as

$$\mathbf{F}(s) = \text{diag}\left(e^{-\imath k_1 s}, \ldots, e^{-\imath k_6 s}\right) \ . \tag{25}$$

Combining Eqs. (25) and (24), one obtains

$$\begin{aligned} \mathbf{a}^+ &= \left[\mathbf{I}_{6\times 6} - \mathbf{F}(s_e)\mathbf{r}_L\mathbf{F}(Npl_2)\mathbf{r}_R\mathbf{F}(Npl_2 - s_e)\right]^{-1}\left[\mathbf{e}^- + \mathbf{F}(s_e)\mathbf{r}_L\mathbf{F}(s_e)\mathbf{e}^-\right] \ , \\ \mathbf{a}^- &= \mathbf{F}(Npl_2 - s_e)\mathbf{r}_R\mathbf{F}(Npl_2 - s_e)\mathbf{a}^+ \ . \end{aligned} \tag{26}$$

The response at any point can be subsequently obtained by finding the wave amplitudes at the location of interest and then using the wave basis of Eq. (21). For example, at s_r, the wave amplitudes are

$$\mathbf{b}^+ = \mathbf{F}(s_r - s_e)\mathbf{a}^+ \quad \text{and} \quad \mathbf{b}^- = \mathbf{F}(Npl_2 - s_r)\mathbf{r}_R\mathbf{F}(Npl_2 - s_r)\mathbf{b}^+ \ . \tag{27}$$

4. Numerical examples

4.1. Benchmark example

Consider a double helical rod with $R_1 = 6.5$ cm, $d/R_1 = 0.184$, $\psi = 0.13$ rad, $\theta = 0$, $R_2 = R_1/10$ and $p = 10$. The non-dimensional frequency is introduced as

$$\Omega = \frac{\omega d}{c} \quad \text{where} \quad c = \sqrt{\frac{E}{\rho}} \ .$$

The FE model of a single turn of the double helical rod is obtained using 41 BEAM188 elements of ANSYS. BEAM188 is a two-noded element with six degrees of freedom per node that is based on the Timoshenko beam theory which includes shear-deformation effects. The length of one turn of the double helical rod can be obtained using Eq. (7); for the values used herein, one can obtain $l_2 = 4.12$ cm. Thus, the obtained stiffness and mass matrices are 252×252. However, when these matrices are reduced as elaborated in Section 3.1.1 , the WFE method is applied to a 12×12 system which represents the degrees of freedom of the end nodes of the turn. The WFE model will have six positive going and six negative going waves. All the waves will be retained in the wave basis presented in Section 3.1.1.

The wavenumbers of a helical rod can be obtained analytically using either the Euler–Bernoulli or Timoshenko beam theories [8]. If $R_2 = 0$, the formulation presented in Section 3.1 will yield the wavenumbers of a helical rod and these can be compared to the analytical dispersion curves of [8]. For this case, the WFE model is obtained using the same segment introduced above (i.e., its length is also l_2). Fig. 5 shows that the WFE computation of the dispersion curves is in very good agreement with the analytical dispersion curves in the low-frequency range. At higher frequencies, Fig. 6, the difference between the WFE model and the analytical dispersion curves becomes more visible. This is due to discretization errors since the size of the segment used in the WFE model is relatively large [22].

Now consider the double helical rod introduced at the beginning of this section. The primary helical path around which the centreline of the double helical rod is coiled has six turns (i.e, $N = 6$) and thus, the double helical rod has 60 turns. The dispersion curves are presented in Figs. 7 and 8. In the low-frequency range, the dispersion curves exhibit clear similarities with the dispersion curves of the helical rod, Fig. 7. At higher frequencies, the double helical rod exhibits stop-pass band behaviour, Fig. 8 that is typical of periodic structures. This is expected since the double helical rod (as elaborated in Section 2 and illustrated in Figs. 3a and 3b) is a periodic rather than a homogeneous waveguide.

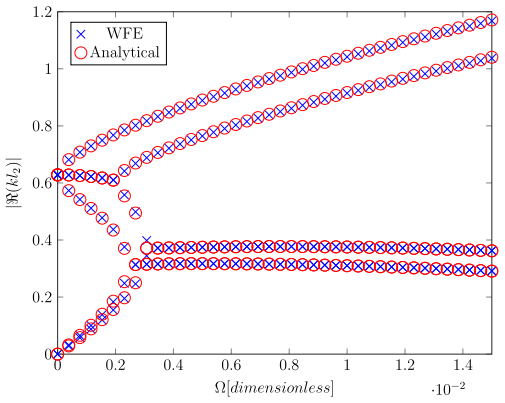

(a) Real part of the (nondimensional) wavenumber.

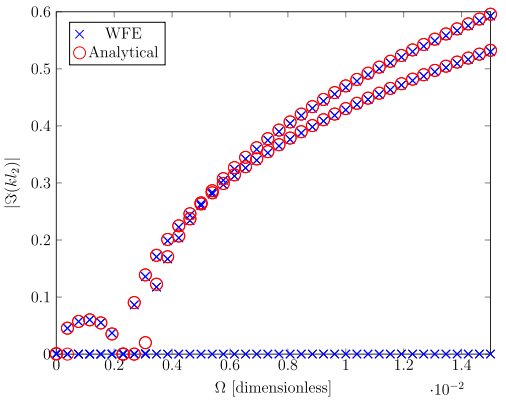

(b) Imaginary part of the (nondimensional) wavenumber.

Fig. 5. Dispersion curves of a helical rod with $R_1 = 6.5$ cm, $d/R_1 = 0.184$, $\psi = 0.13$ rad and $R_2 = 0$ in the low-frequency range.

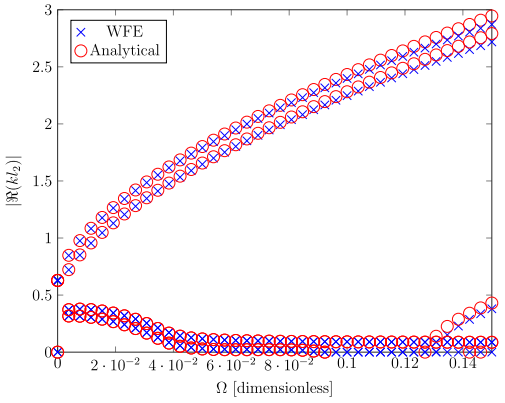

(a) Real part of the (nondimensional) wavenumber.

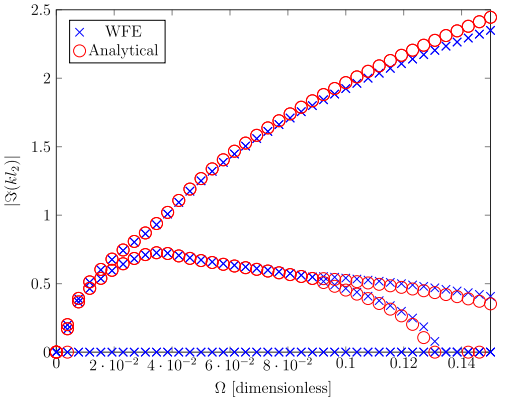

(b) Imaginary part of the (nondimensional) wavenumber.

Fig. 6. Dispersion curves of a helical rod with $R_1 = 6.5$ cm, $d/R_1 = 0.184$, $\psi = 0.13$ rad and $R_2 = 0$ in the high frequency range.

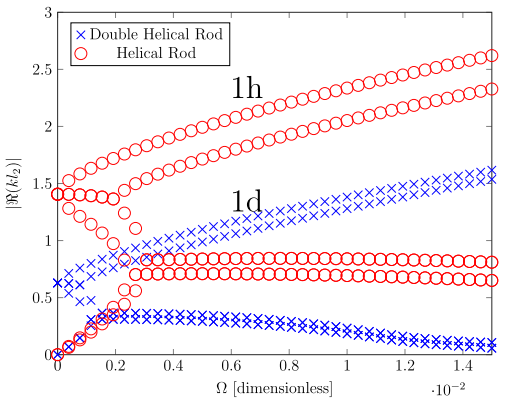

(a) Real part of the (nondimensional) wavenumber.

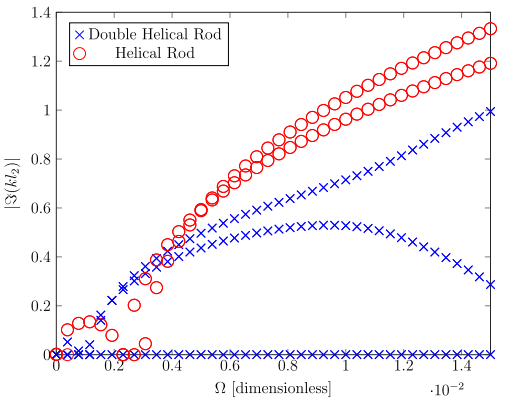

(b) Imaginary part of the (nondimensional) wavenumber.

Fig. 7. Dispersion curves of a double helical rod with $R_1 = 6.5$ cm, $d/R_1 = 0.184$, $\psi = 0.13$ rad and $R_2 = R_1/5$ in the low-frequency range. The annotated wavenumber branches will be discussed in Section 4.2.

To ensure that the developed model is robust, the double helical rod is fixed at one end and a time harmonic force in the global z direction is applied at the free end. The input mobility obtained by Sections 3.2 and 3.3 is compared to a full

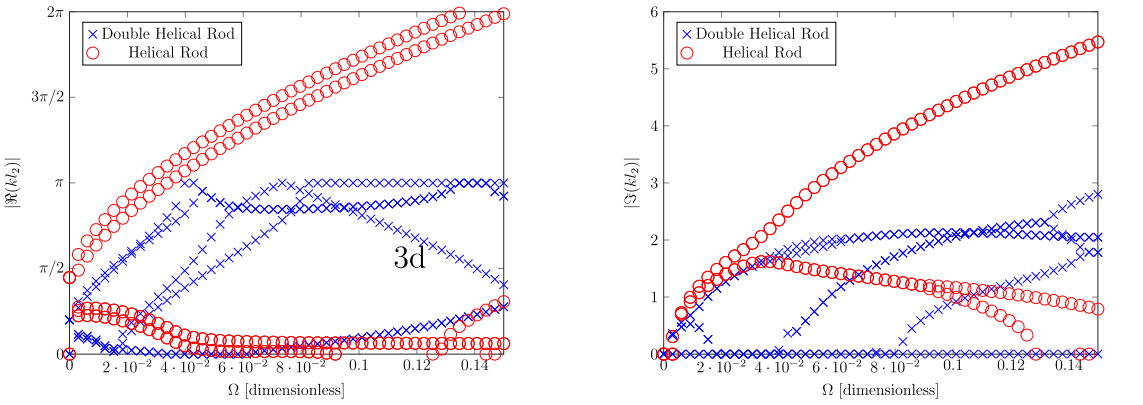

(a) Real part of the (nondimensional) wavenumber. (b) Imaginary part of the (nondimensional) wavenumber.

Fig. 8. Dispersion curves of a double helical rod with $R_1 = 6.5$ cm, $d/R_1 = 0.184$, $\psi = 0.13$ rad and $R_2 = R_1/5$ in the high-frequency range. The annotated wavenumber branches will be discussed in Section 4.2.

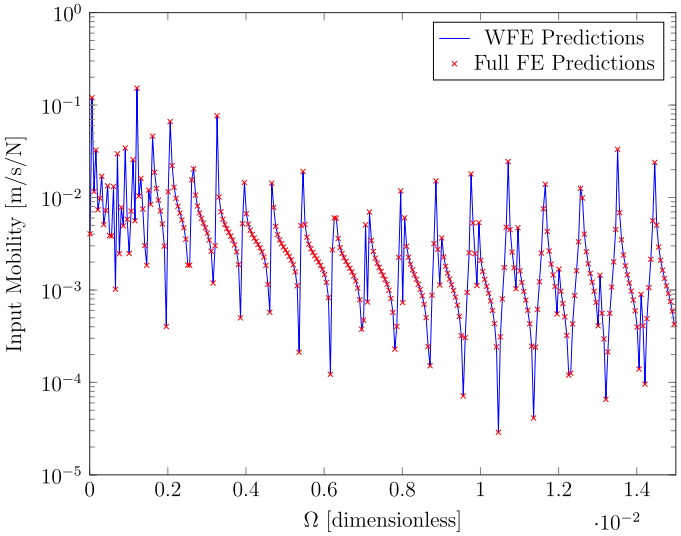

Fig. 9. Input mobility of the double helical rod in the low-frequency range.

FE prediction in Figs. 9 and 10. At low and high frequencies, the predictions of the WFE method are in excellent agreement with the full FE predictions. The WFE uses only six pairs of waves to obtain the solution whereas the computational cost of the FE model is certainly higher (even if modal superposition is used). The computation time will depend on the number of turns of the double helical rod. As the double helical rod becomes longer, its FE model will increase in size whereas the WFE model will remain the same. In particular, the only modification to the WFE predictions will be in Eqs. (26) and (27) which does not add any computational cost to the WFE model. The effect of the band gaps presented in Fig. 8a can be observed in Fig. 10 where the input mobility is lower at the band gaps (e.g. when $\Omega \approx 4 \times 10^{-2}$ and when $\Omega \approx 0.13$).

4.2. Analysis of wavemodes

In this section, the wave behaviour of the double helical rod will be analysed and the wavemodes will be examined. Figs. 11 and 12 show the dispersion curves of the double helical rod with varying values of R_2. Fractal effects are evident in Fig. 11 where the behaviour of the helical rod is indicated by $R_2 = 0$ and forms the original pattern that is followed and scaled down by the dispersion curves of the double helical rod with varying R_2 values. Thus, as the double helical rod is a helix coiled around another helix, the dispersion curves of the double helical rod follow the same shape of those of the helical rod but at lower values. The component of the wave modes will be similar; however, the three-dimensional behaviour of the double helical waveguide will be different than that of the helical waveguide under the same wavemode and at the same frequency due to the markedly different geometric coupling in the double helical rod.

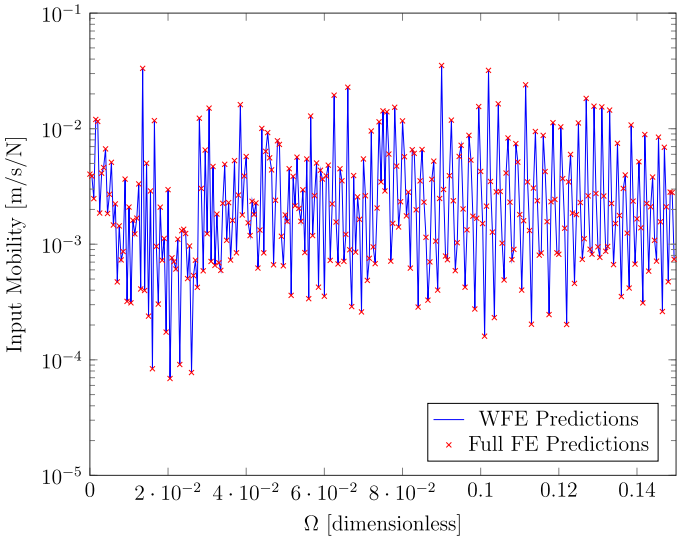

Fig. 10. Input mobility of the double helical rod in the high-frequency range.

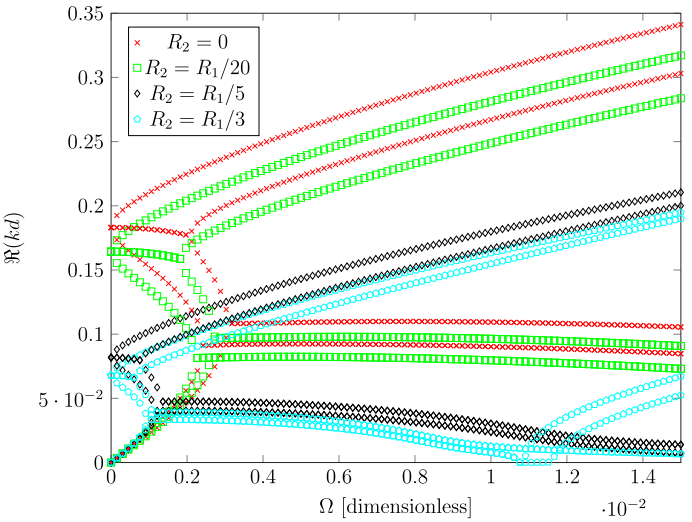

Fig. 11. Demonstration of the fractal effect in the dispersion curves of a double helical rod — real part of the nondimensional wavenumber.

As for the wavemodes, these can be obtained from the eigenvalue problem of Eq. (18) where the vector of DOFs under the ith wave is $\mathbf{q}_L^{(i)} = \{\boldsymbol{\phi}_q\}_i$ (Eq. (19)). The motion of each turn of the double helical rod under the ith wave can be obtained as

$$\mathbf{q}_R^{(i)} = \exp(-\imath k_i^+ l_2)\mathbf{q}_L^{(i)} \quad \text{and} \quad \mathbf{q}_I^{(i)} = -\tilde{\mathbf{D}}_{II}^{-1}\left[\tilde{\mathbf{D}}_{IL}\mathbf{q}_L^{(i)} + \tilde{\mathbf{D}}_{IR}\mathbf{q}_R^{(i)}\right] . \tag{28}$$

Fig. 13 shows the wavemodes of the helical rod and double helical rod under wavenumber branches 1h and 1d (which are annotated in Fig. 7). Fig. 13a is a bending wave that propagates along the helical rod. The same bending behaviour is observed in Fig. 13b where the bending wave propagates along the double helical rod.

The wavemode obtained in Eq. (28) is a vector of DOFs comprising three displacement DOFs and three rotational DOFs along and about the local coordinates $(\hat{t}_1, \hat{n}_1, \hat{n}_1)$ (for the helical rod) and $(\hat{t}_2, \hat{n}_2, \hat{n}_2)$ (for the double helical rod) that were introduced in Section 2. Fig. 14 shows the time history (over one period at $\Omega = 0.015$) of the displacement DOFs of $\mathbf{q}_L^{(i)} \exp(-\imath\omega t)$. The vector of the three displacements is normalized to the maximum displacement in order to compare the displacements in Fig. 14 can be easily compared. Although the displacement DOFs of these two wavemodes are not very different from each other as demonstrated in Fig. 14, the wavemodes are quite different as demonstrated in Fig. 13. Branch 1h (for the helical rod) is primarily a bending wave that propagates along the helical rod with components in all

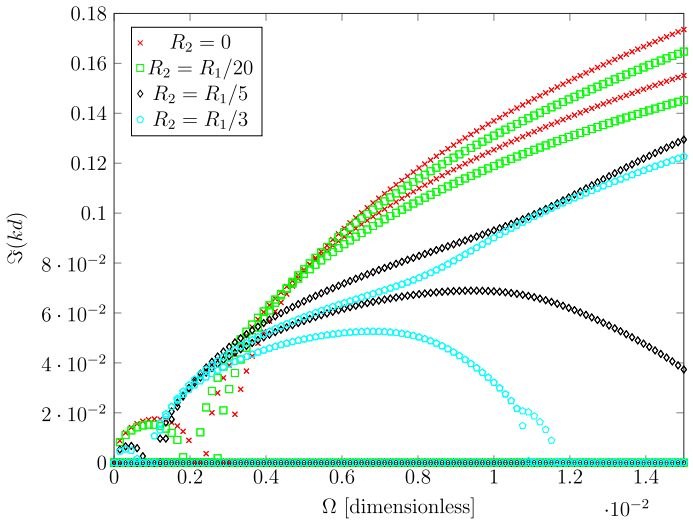

Fig. 12. Demonstration of the fractal effect in the dispersion curves of a double helical rod — imaginary part of the nondimensional wavenumber.

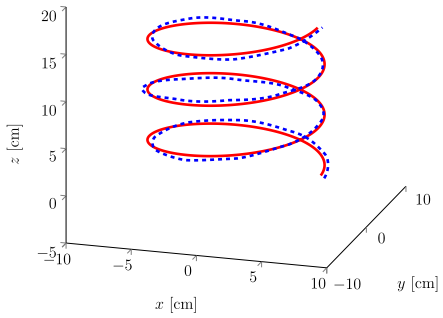

(a) Motion of the helical rod under wavenumber branch 1h (Figure 7).

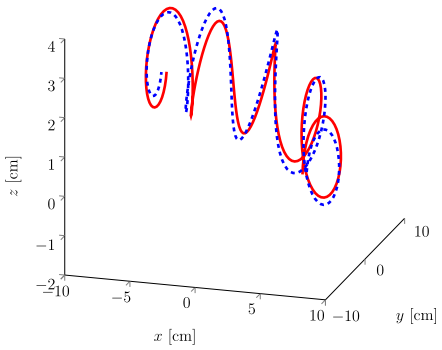

(b) Motion of the double helical rod under wavenumber branch 1d (Figure 7).

Fig. 13. Wave modes at $\Omega = 0.005$ (solid line is un-deformed rod, and dashed line represents the deformed rod).

local coordinates. However, due to the varying spatial variation of the tortuosity and curvature of the double helical rod, wavemode 1d is demonstrated as expansion of the turns of the helical rod.

At higher frequencies, Fig. 8a, the wavemodes of the double helical rod will have periodic and localized behaviour. Fig. 15 shows a section of the double helical rod where each turn of the double helical rod will undergo localized radial motion.

5. Conclusion

Although the modelling of wave propagation in double helical rods did not receive enough attention, it can be useful in multiple fields of science and engineering ranging from understanding biological structures to advancing the understanding of string theory. In this paper, a double helical rod is modelled using the wave and finite element (WFE). The double helical rod is not a homogeneous waveguide; it is rather a periodic waveguide whose period is a single turn of the secondary helix. A single turn of the double helical rod is modelled using beam elements from a commercial FE software package. Bloch waves are used to formulate an eigenvalue problem whose solutions are the dispersion curves and wavemodes of the double helical rod. Compared to the dispersion curves of a helical rod, the dispersion curves of the double helical rod demonstrate fractal effects. Despite the similarity in the dispersion curves, the wave modes are quite different even in the low-frequency range. This is mainly due to the spatial variation of the curvature and the tortuosity of the double helical rod. In the high-frequency range, the wavemodes are localized (i.e., in each turn of the double helical rod) which reflects the periodic nature of the double helical rod. The work presented herein can be extended to study the wave behaviour of double helical waveguides which can be more representative of molecular structures.

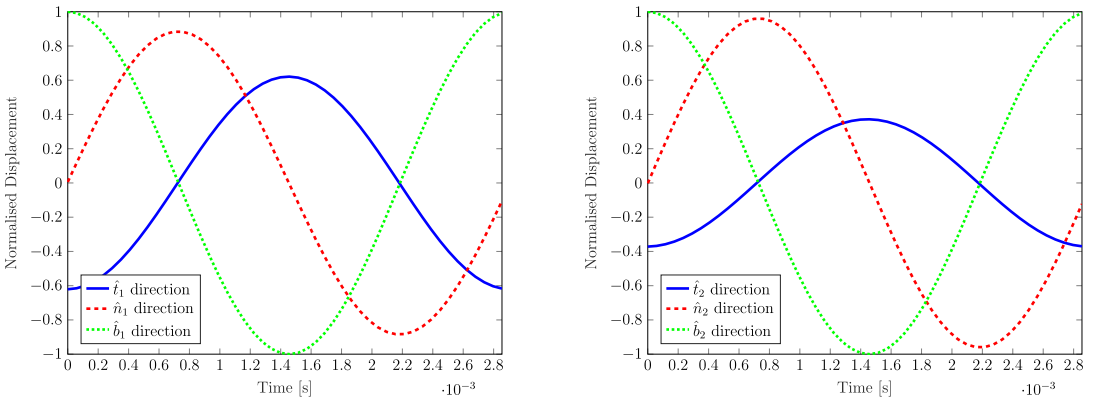

(a) Wavenumber branch 1h at $\Omega = 0.005$. (b) Wavenumber branch 1d at $\Omega = 0.005$.

Fig. 14. Normalized displacement of wavemodes simulated over one period.

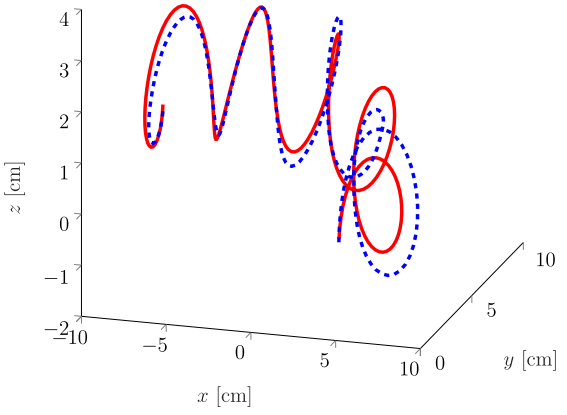

Fig. 15. Motion of the helical rod under wavenumber branch 3d at $\Omega = 0.1$ (Fig. 8a).

Acknowledgements

The authors gratefully acknowledge the financial support provided by the Qatar National Research Fund through the National Priorities Research Program under grant number NPRP 11S-1220-170112 and Qatar University Internal Grant QUCG-CENG-19/20-6.

Appendix. Curvature of the double helix

The curvature of the double helix can be obtained as

$$\kappa_2(s) = \sqrt{\frac{N(s)}{D(s)}}\,. \tag{A.1}$$

The numerator, $N(s)$, is

$$\begin{aligned} N(s) \;=\; & 4c_{2,2}\kappa_1^2 R_2^2 N_1 - 8c_{2,1}\kappa_1 R_2 N_2 + N_3 - 8c_{2,3}\kappa_1^3 R_2^3 \tau_1 \epsilon_2 + c_{2,4}\kappa_1^4 R_2^4 \tau_1^2 \\ & -8c_{2,3}\kappa_1^3 R_2^3 \tau_1^2 - c_{2,4}\kappa_1^4 R_2^4 \epsilon_2^2 + c_{2,4}\kappa_1^6 R_2^4 - 8c_{2,3}\kappa_1^5 R_2^3 \end{aligned} \tag{A.2}$$

where

$$c_{2,i} = \cos\left[i(\epsilon_2 s + \theta)\right] \quad \text{and} \quad s_{2,i} = \sin\left[i(\epsilon_2 s + \theta)\right] \quad i = 1, 2, \ldots\,.$$

The constants N_1, N_2 and N_3 are

$$\begin{aligned} N_1 &= 3\kappa_1^2\left(2R_2^2\tau_1\epsilon_2 + R_2^2\tau_1^2 + R_2^2\epsilon_2^2 + 2\right) + \kappa_1^4 R_2^2 \\ &\quad -(\tau_1+\epsilon_2)\left(-4R_2^2\tau_1^2\epsilon_2 - R_2^2\tau_1\epsilon_2^2 - 2R_2^2\tau_1^3 + R_2^2\epsilon_2^3 - 5\tau_1 - 3\epsilon_2\right) , \end{aligned} \tag{A.3}$$

$$\begin{aligned} N_2 &= \kappa_1^2\left(15R_2^2\tau_1\epsilon_2 + 7R_2^2\tau_1^2 + 8R_2^2\epsilon_2^2 + 4\right) + 3\kappa_1^4 R_2^2 \\ &\quad +2\left(\tau_1+\epsilon_2\right)^2\left(4R_2^2\tau_1\epsilon_2 + 2R_2^2\tau_1^2 + 2R_2^2\epsilon_2^2 + 1\right) , \end{aligned} \tag{A.4}$$

$$\begin{aligned} N_3 &= 8\kappa_1^2 + 24\kappa_1^4 R_2^4\tau_1\epsilon_2 + 96\kappa_1^2 R_2^4\tau_1\omega_2^3 + 124\kappa_1^2 R_2^4\tau_1^2\epsilon_2^2 + 72\kappa_1^2 R_2^4\tau_1^3\epsilon_2 + 80\kappa_1^2 R_2^2\tau_1\epsilon_2 \\ &\quad +11\kappa_1^4 R_2^4\tau_1^2 + 16\kappa_1^2 R_2^4\tau_1^4 + 36\kappa_1^2 R_2^2\tau_1^2 + 13\kappa_1^4 R_2^4\epsilon_2^2 + 28\kappa_1^2 R_2^4\epsilon_2^4 + 44\kappa_1^2 R_2^2\epsilon_2^2 + 3\kappa_1^6 R_2^4 \\ &\quad +24\kappa_1^4 R_2^2 + 48R_2^4\tau_1\epsilon_2^5 + 120R_2^4\tau_1^2\epsilon_2^4 + 160R_2^4\tau_1^3\epsilon_2^3 + 32R_2^2\tau_1\epsilon_2^3 + 120R_2^4\tau_1^4\epsilon_2^2 \\ &\quad +48R_2^2\tau_1^2\epsilon_2^2 + 48R_2^4\tau_1^5\epsilon_2 + 32R_2^2\tau_1^3\epsilon_2 + 8R_2^4\tau_1^6 + 8R_2^2\tau_1^4 + 8R_2^4\epsilon_2^6 + 8R_2^2\epsilon_2^4 . \end{aligned} \tag{A.5}$$

The denominator in Eq. (A.1), $D(s)$, is given as

$$D(s) = 2\left(c_{2,2}\kappa_1^2 R_2^2 - 4c_{2,1}\kappa_1 R_2 + \kappa_1^2 R_2^2 + 4R_2^2\tau_1\epsilon_2 + 2R_2^2\tau_1^2 + 2R_2^2\epsilon_2^2 + 2\right)^2 \tag{A.6}$$

If $R_2 = 0$ (i.e., the double helix is reduced to the primary helix), then $N(s) = 8\kappa_1^2$ and $D(s) = 8$, which retrieves the curvature of the primary helix with $\kappa_2 = \kappa_1$.

References

[1] A. Love, The propagation of waves of elastic displacement along a helical wire, Trans. Cambridge Philos. Soc. 18 (1899) 364–374.
[2] W. Wittrick, On elastic wave propagation in helical springs, Int. J. Mech. Sci. 8 (1) (1966) 25–47.
[3] J. Mottershead, Finite elements for dynamical analysis of helical rods, Int. J. Mech. Sci. 22 (5) (1980) 267–283.
[4] J. Lee, D. Thompson, Dynamic stiffness formulation, free vibration and wave motion of helical springs, J. Sound Vib. 239 (2) (2001) 297–320.
[5] J. Lee, Free vibration analysis of cylindrical helical springs by the pseudospectral method, J. Sound Vib. 302 (1–2) (2007) 185–196.
[6] F. Treyssède, Numerical investigation of elastic modes of propagation in helical waveguides, J. Acoust. Soc. Am. 121 (6) (2007) 3398–3408.
[7] F. Treyssède, Elastic waves in helical waveguides, Wave Motion 45 (4) (2008) 457–470.
[8] S. Sorokin, Linear dynamics of elastic helical springs: Asymptotic analysis of wave propagation, Proc. R. Soc. A 465 (2105) (2009) 1513–1537.
[9] S. Sorokin, The green's matrix and the boundary integral equations for analysis of time-harmonic dynamics of elastic helical springs, J. Acoust. Soc. Am. 129 (3) (2011) 1315–1323.
[10] Y. Liu, Q. Han, C. Li, H. Huang, Numerical investigation of dispersion relations for helical waveguides using the scaled boundary finite element method, J. Sound Vib. 333 (7) (2014) 1991–2002.
[11] F. Maurin, C. Claeys, L. Van Belle, W. Desmet, Bloch theorem with revised boundary conditions applied to glide, screw and rotational symmetric structures, Comput. Methods Appl. Mech. Engrg. 318 (2017) 497–513.
[12] N. Fletcher, T. Tarnopolskaya, F. de Hoog, Wave propagation on helices and hyperhelices: a fractal regression, Proc. R. Soc. A 457 (2005) (2001) 33–43.
[13] S. Furois-Corbin, J. Smith, G. Kneller, Picosecond timescale rigid-helix and side-chain motions in deoxymyoglobin, Proteins: Struct. Funct. Bioinform. 16 (2) (1993) 141–154.
[14] S. Furois-Corbin, J. Smith, R. Lavery, Low-frequency vibrations in α-helices: Helicoidal analysis of polyalanine and deoxymyoglobin molecular dynamics trajectories, Biopolymers 35 (6) (1995) 555–571.
[15] N. Fletcher, Hyperhelices: A classical analog for strings and hidden dimensions, Amer. J. Phys. 72 (5) (2004) 701–703.
[16] Y. Zhang, Z. Liu, L. Shen, J. Qian, Detection of pipeline curvature with fbg sensors twisted, Appl. Mech. Mater. 303–306 (2013) 67–73.
[17] L. Zhang, J. Qian, Y. Zhang, L. Shen, On sdm/wdm fbg sensor net for shape detection of endoscope, 2005, pp. 1986–1991.
[18] J. Moore, M. Rogge, Shape sensing using multi-core fiber optic cable and parametric curve solutions, Opt. Express 20 (3) (2012) 2967–2973.
[19] S. Lim, S. Han, Series representations for the rectification of a superhelix, Appl. Math. Model. 56 (2018) 381–388.
[20] B. Mace, D. Duhamel, M. Brennan, L. Hinke, Finite element prediction of wave motion in structural waveguides, J. Acoust. Soc. Am. 117 (5) (2005) 2835–2843.
[21] D. Duhamel, B. Mace, M. Brennan, Finite element analysis of the vibrations of waveguides and periodic structures, J. Sound Vib. 294 (1–2) (2006) 205–220.
[22] Y. Waki, B.R. Mace, M.J. Brennan, Numerical issues concerning the wave and finite element method for free and forced vibrations of waveguides, J. Sound Vib. 327 (1–2) (2009) 92–108.
[23] J.M. Renno, B.R. Mace, On the forced response of waveguides using the wave and finite element method, J. Sound Vib. 329 (26) (2010) 5474–5488.
[24] G. Mitrou, N. Ferguson, J. Renno, Wave transmission through two-dimensional structures by the hybrid FE/WFE approach, J. Sound Vib. 389 (2017) 484–501.
[25] E. Manconi, S. Sorokin, R. Garziera, A. Soe-Knudsen, Wave motion and stop-bands in pipes with helical characteristics using wave finite element analysis, J. Appl. Comput. Mech. 4 (2018) 420–428.
[26] S. Sorokin, E. Manconi, L. Ledet, R. Garziera, Wave propagation in helically orthotropic elastic cylindrical shells and lattices, Int. J. Solids Struct. 170 (2019) 11–21.
[27] Wolfram Research, Inc., Mathematica 11.3. URL https://www.wolfram.com.
[28] J.-M. Mencik, New advances in the forced response computation of periodic structures using the wave finite element (WFE) method, Comput. Mech. 54 (3) (2014) 789–801.
[29] Y. Waki, B.R. Mace, M.J. Brennan, Free and forced vibrations of a tyre using a wave/finite element approach, J. Sound Vib. 323 (3–5) (2009) 737–756.

[30] J. Renno, B. Mace, Vibration modelling of helical springs with non-uniform ends, J. Sound Vib. 331 (12) (2012) 2809–2823.
[31] J. Renno, N. Søndergaard, S. Sassi, M.R. Paurobally, Wave scattering and power flow in straight-helical-straight waveguide structure, Int. J. Appl. Mech. 11 (8) (2019).
[32] W. Zhong, F. Williams, On the direct solution of wave propagation for repetitive structures, J. Sound Vib. 181 (3) (1995) 485.
[33] B.R. Mace, Wave reflection and transmission in beams, J. Sound Vib. 72 (2) (1984) 237–246.